PNAS

Partial PdAu nanoparticle embedding into TiO_2 support accentuates catalytic contributions from the Au/TiO_2 interface

Kang Rui Garrick Lim[1,2], Selina K. Kaiser[1,2], Connor J. Herring[3], Taek-Seung Kim[4], Marta Perxés Perich[5], Sadhya Garg[2], Christopher R. O'Connor[4], Michael Aizenberg[2], Jessi E. S. van der Hoeven[5], Christian Reece[4], Matthew M. Montemore[3], Joanna Aizenberg[1,2,*]

[1] Department of Chemistry and Chemical Biology, Harvard University, Cambridge, Massachusetts 02138, United States

[2] John A. Paulson School of Engineering and Applied Sciences, Harvard University, Cambridge, Massachusetts 02138, United States

[3] Department of Chemical and Biomolecular Engineering, Tulane University, New Orleans, Louisiana 70118, United States

[4] Rowland Institute at Harvard, Harvard University, Cambridge, Massachusetts 02142, United States

[5] Materials Chemistry and Catalysis, Debye Institute for Nanomaterials Science, Utrecht University, 3584 CG Utrecht, Netherlands

* Corresponding author. Email: jaiz@seas.harvard.edu (J. A.)

Author Contributions: K.R.G.L., S.K.K., M.A., and J.A. designed research. K.R.G.L., S.K.K., C.J.H., T.-S.K., M.P.P., S.G., C.R.O., and J.E.S.v.d.H. performed research and analyzed data. K.R.G.L., M.A., and J.A. wrote the paper. M.A., J.E.S.v.d.H., C.R., M.M.M., and J.A. supervised research. J.A. supervised the entire work.

Data Availability: All data that support this work are available in the main text and Supporting Information.

Competing Interest: Christian Reece and Graham Hutchings participated in a Faraday Discussion together in 2021 (*Faraday Discuss.* **229**, 378–421 (2021)).

Classification: Physical Sciences (Chemistry)

Keywords: Metal–support interface, catalyst design, nanoparticle embedding, interfacial catalysis, hydrogenation

This PDF file includes: Main Text, Figures 1 to 5

Abstract

Despite the broad catalytic relevance of metal–support interfaces, controlling their chemical nature, interfacial contact perimeter (exposed to reactants), and consequently, their contributions to overall catalytic reactivity, remains challenging as the nanoparticle and support characteristics are interdependent when catalysts are prepared by impregnation. Here, we decoupled both characteristics by using a raspberry-colloid-templating (RCT) strategy that yields partially embedded PdAu nanoparticles within well-defined SiO_2 or TiO_2 supports, thereby increasing the metal–support interfacial contact compared to non-embedded catalysts that we prepared by attaching the same nanoparticles onto support surfaces. Between non-embedded PdAu/SiO_2 and PdAu/TiO_2, we identified a support effect resulting in a 1.4-fold higher activity of PdAu/TiO_2 than PdAu/SiO_2 for benzaldehyde hydrogenation. Notably, partial nanoparticle embedding in the TiO_2 RCT support increased the metal–support interfacial perimeter and consequently, the number of Au/TiO_2 interfacial sites by 5.4-fold, which further enhanced the activity of PdAu/TiO_2 by an additional 4.1-fold. Theoretical calculations and *in situ* surface-sensitive desorption analyses reveal facile benzaldehyde binding at the Au/TiO_2 interface and at Pd ensembles on the nanoparticle surface, explaining the connection between the number of Au/TiO_2 interfacial sites (*via* the metal–support interfacial perimeter) and catalytic activity. Our results demonstrate partial nanoparticle embedding as a synthetic strategy to produce thermocatalytically stable catalysts and increase the number of catalytically active Au/TiO_2 interfacial sites to augment catalytic contributions arising from metal–support interfaces.

Significance Statement

Most supported catalysts are produced by forming or attaching nanoparticles onto surfaces of supports. However, controlling the interfacial contact between the nanoparticles and support—which has been reported to be the active site for many catalytic reactions—remains synthetically challenging. Here, we employ a colloidal templating approach to derive catalysts comprising PdAu nanoparticles partially embedded within SiO_2 or TiO_2 supports. Compared to a conventional catalyst prepared by attaching PdAu nanoparticles onto TiO_2 surfaces, partial entrenchment of nanoparticles into TiO_2 increased the nanoparticle–support interfacial perimeter and enhanced the catalytic activity by 4.1-fold. Our results illustrate partial nanoparticle embedding as a synthetic strategy to increase the number of Au/TiO_2 interfacial sites and amplify their catalytic contributions, while enhancing catalyst stability.

Introduction

Metal–support interfaces are found in practically all nanoparticle (NP)-supported catalysts and their interactions are relevant for a wide range of catalytic reactions (1–4). While conventionally impregnated catalysts have tuned NP–support interactions to some extent by changing the size of NPs (5, 6) or support grains (7), this approach is not best suited for investigations between different support chemistries. This is because in impregnation, the support chemistry strongly influences NP nucleation characteristics (*e.g.,* size, shape, or dispersion) (8–10) and *vice versa*, thus precluding independent variation to isolate catalytic effects arising solely from NP–support interactions. Traditional catalyst preparation methods also directly form NPs attached on support surfaces and consequently, limit our ability to control or manipulate the NP–support interfacial contact (11). Additionally, under thermocatalytic conditions of high temperature, pressure, and mechanical agitation, conventionally prepared catalysts are prone to NP leaching and sintering that further confounds catalytic analyses (12, 13).

To address these limitations, we, together with other researchers, have identified partial NP embedding into the support as a key design feature to increase the NP–support interfacial perimeter and improve catalyst stability against sintering (14–17). Synthetic strategies to achieve partial NP embedding include NP exsolution from metal-doped supports (18–20) and the encapsulation of NPs by metal oxides by inverted catalyst designs (15, 21–23) or through strong metal–support interactions (2, 4, 24). However, these approaches are still restricted to specific metal–support combinations due to the same high degree of NP–support interdependence intrinsic to impregnation methods (18, 20, 23). For instance, classical strong metal–support interactions to induce metal oxide overgrowth around NPs typically occur only in reductive reaction environments and on reducible metal oxide supports (24). Moreover, tailoring the NP size and composition of multi-metallic NPs remains a long-standing challenge in exsolution (18, 20). Finally, synthetic control over NP embedding levels in all these strategies requires delicate synthetic control to avoid full NP encapsulation and preserve sufficient reactant accessibility (16, 23).

Here, we adapted our modular raspberry-colloid-templating (RCT) strategy (25, 26) that decouples the NP and support formation steps to partially embed pre-formed PdAu NPs of a fixed size in well-defined SiO_2 or TiO_2 supports to systematically study effects arising from NP–support interfaces. When tested using benzaldehyde hydrogenation as our probe reaction, the partially embedded $Pd_{13}Au_{87}/TiO_2$ RCT catalysts was 4.1-fold more active than conventional non-embedded $Pd_{13}Au_{87}/TiO_2$ catalysts prepared by attaching the same NPs onto surfaces of morphologically identical TiO_2. *In situ* surface-sensitive desorption analyses and theoretical calculations indicate benzaldehyde binding on both Pd ensembles and Au/TiO_2 interfaces, explaining the relationship between Au/TiO_2 interfacial perimeter and activity. Our results demonstrate partial NP embedding as a synthetic

strategy to augment the number of Au/TiO_2 interfacial sites to facilitate additional benzaldehyde binding and thus, amplify its catalytic contributions to overall activity, while enhancing catalytic stability. This work also presents the modular RCT method as a model catalyst platform to unambiguously compare NP–support interfacial effects between supports without being confounded by concomitant changes to other physicochemical properties (*e.g.,* NP size (9, 27, 28), proximity (29), or composition (30)) that may act as potential catalytic descriptors.

Results and Discussion

Preparation of partially embedded and non-embedded catalysts. We adapted a modular RCT strategy to prepare catalysts comprising uniformly-sized $Pd_{13}Au_{87}$ NPs partially embedded in either a SiO_2 or TiO_2 support (**Fig. 1a**) (25). The Au-rich $Pd_{13}Au_{87}$ NP composition was selected so that Au/SiO_2 or Au/TiO_2 sites would be abundant at the NP–support interface, while Pd would accelerate H_2 activation for hydrogenation (30–32). The two supports were chosen to compare the Au/SiO_2 interface, which we earlier reported to be inactive for benzaldehyde hydrogenation (our probe reaction) (30–32), against the Au/TiO_2 interface, which we hypothesize might be active for the same reaction, given earlier reports of nitro group hydrogenation by Au/TiO_2 (33, 34). Apart from these partially embedded RCT catalysts, we also prepared two sets of controls. First, to evaluate the effect of partial NP embedding on catalytic performance, we prepared non-embedded catalysts by immobilizing the same pre-formed $Pd_{13}Au_{87}$ NPs onto the surfaces of morphologically identical SiO_2 or TiO_2 supports (**Fig. 1b**). For clarity, we refer to the partially embedded RCT catalysts as $Pd_{13}Au_{87}$/support-RCT, and the non-embedded catalysts as $Pd_{13}Au_{87}$/support-attached. Second, to ensure that our subsequent catalytic findings were not specific to the $Pd_{13}Au_{87}$ NP composition, we exploited the synthetic flexibility of the RCT method (25) to prepare RCT catalysts with a range of other monometallic (Au and Pd) and bimetallic Pd_xAu_{100-x} NP compositions (x = 4–13, **Fig. S1a–e**). Across the entire Pd_xAu_{100-x} NP composition series we prepared, the experimentally determined Pd and Au content corroborated well with their expected values from the ratio of Pd to Au metal precursors used during synthesis (by elemental analysis in **Table S1a**).

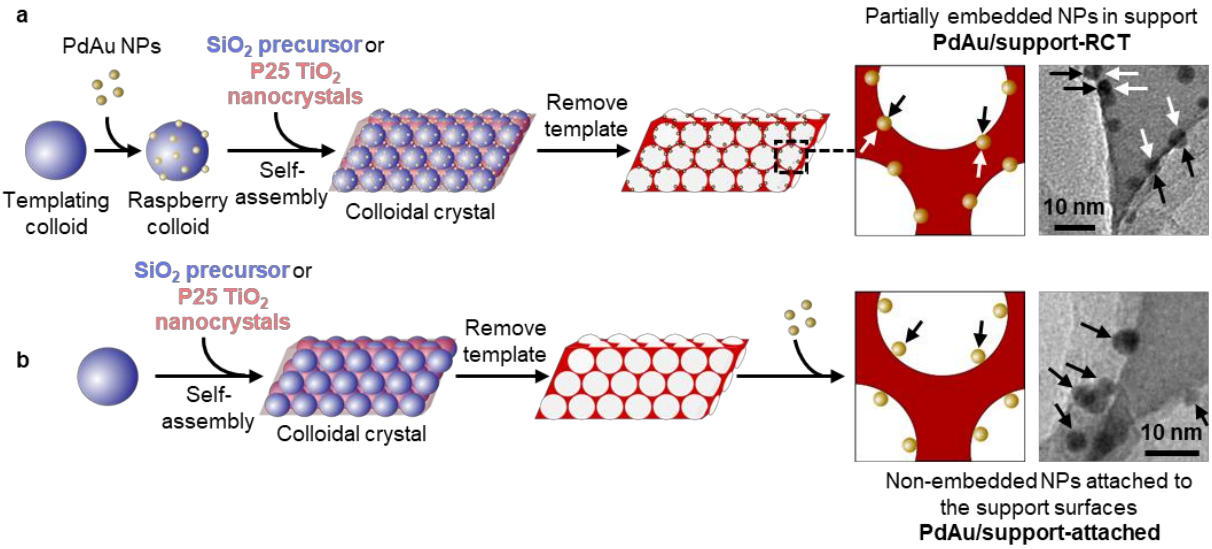

Fig. 1: Synthetic scheme to prepare partially embedded RCT catalysts and non-embedded catalysts. (a) RCT catalysts were prepared by attaching pre-formed colloidal NPs (*e.g.*, $Pd_{13}Au_{87}$) to polymeric templating colloids to form NP-decorated raspberry colloids. The raspberry colloids were self-assembled and infiltrated with a SiO_2 sol-gel precursor (28–30), or co-assembled with P25 TiO_2 nanocrystals (17, 35), forming a colloidal crystal. The colloidal crystal was calcined to remove the polymeric templating colloids and alloy the NPs to yield a 3D macroporous RCT catalyst with NPs partially embedded within the SiO_2 or TiO_2 support (14). (b) Non-embedded catalysts were prepared in a similar manner as the RCT catalysts, except for using NP-free templating colloids instead of NP-decorated raspberry colloids in the self-assembly step. After calcination to form a 3D macroporous SiO_2 or TiO_2 structure, the same pre-formed colloidal NPs were immobilized onto the SiO_2 or TiO_2 support surfaces by infiltration, followed by thermal treatment at the same temperature to homogeneously alloy the NPs. Insets show transmission electron microscopy (TEM) images with (a) NPs partially embedded in the SiO_2 support and (b) fully exposed NPs on surfaces of the macroporous SiO_2 support. White and black arrows indicate segments of the NP surface that are embedded (in the support) and non-embedded (*i.e.,* exposed to reactants), respectively.

For a fair comparison within and between the RCT and non-embedded catalysts, we had to ensure that the catalysts were similar apart from the support chemistry. Indeed, in the RCT catalysts, we observed no physicochemical differences between $Pd_{13}Au_{87}/SiO_2$-RCT and $Pd_{13}Au_{87}/TiO_2$-RCT in terms of macroscopic structure (**Fig. 2a–b**), NP size (≈7 nm, **Fig. 2a insets**), NP elemental distribution (homogeneous PdAu alloys, **Fig. 2c, S1f**), and NP composition (≈13 atomic % Pd at the bulk level in **Table S1a**, ≈14 atomic % Pd at the NP surface level in **Table S1b**). Partial NP embedding in the RCT catalysts was verified by electron tomography of SiO_2-supported (as characterized extensively in our earlier work (14)) and TiO_2-supported RCT catalysts (**Fig. S2, Movie S1**). NP accessibility levels were comparable between SiO_2- and TiO_2-supported RCT catalysts by CO chemisorption analysis which recorded similar amounts of CO uptake and normalized metallic surface areas (**Table S2**). X-ray photoelectron spectroscopy (XPS) analysis of the bimetallic $Pd_{13}Au_{87}$ catalysts revealed that Au and Pd existed in their metallic forms regardless of support chemistry (**Fig. S3**) (28, 29, 36). In the non-embedded catalysts, we found that

while the ordered macroporous support structure was retained (**Fig. 2d, S4**), slight NP sintering had occurred (≈8 nm, **Fig. 2d insets**), emphasizing the importance of partial NP embedding in the RCT method to enhance thermomechanical stability for catalysis (14, 29, 37). The largely comparable physicochemical properties between the RCT and non-embedded catalysts thus facilitated a fair comparison of their catalytic performance.

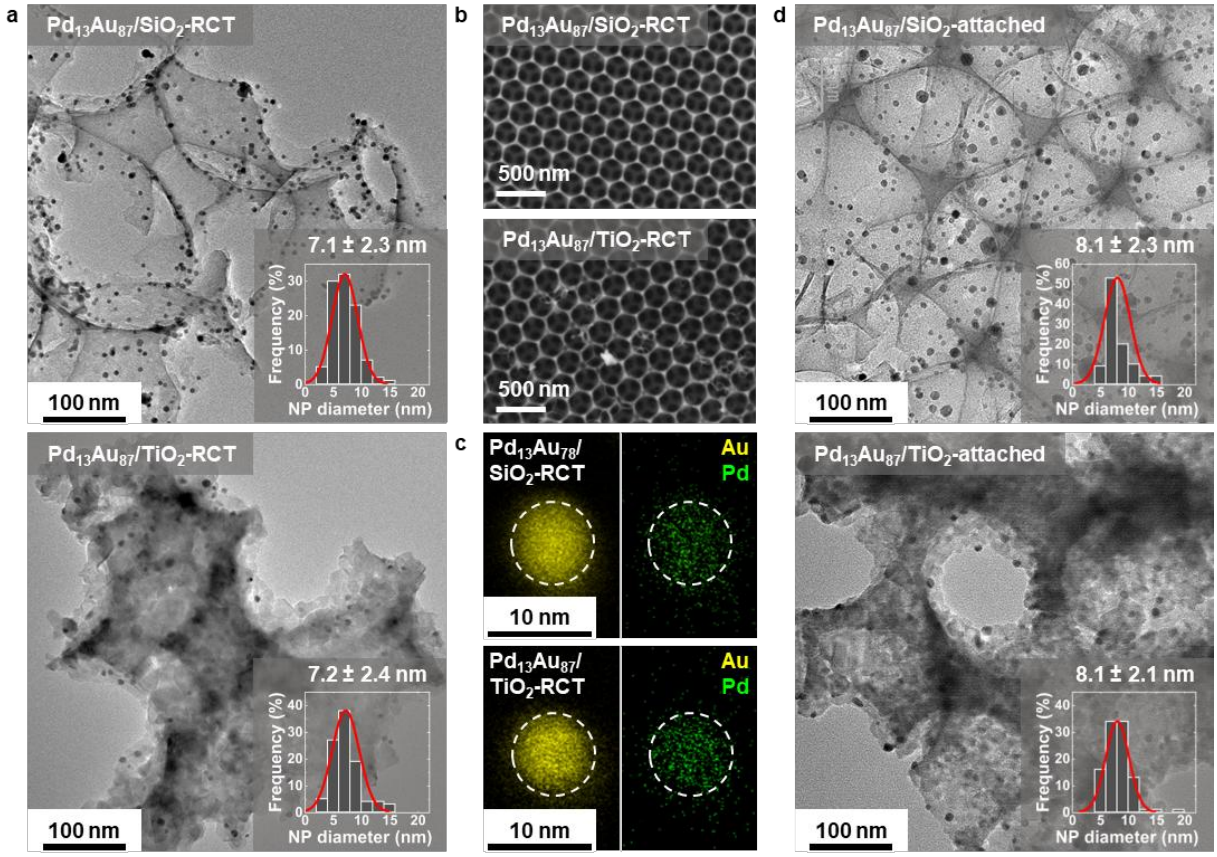

Fig. 2: Electron microscopy of partially embedded RCT catalysts and non-embedded catalysts. (a) Transmission electron microscopy (TEM) and (b) scanning electron microscopy (SEM) images of partially embedded $Pd_{13}Au_{87}/SiO_2$-RCT and $Pd_{13}Au_{87}/TiO_2$-RCT catalysts, depicting their highly ordered 3D macroscopic structure. (c) Scanning transmission electron microscopy-elemental dispersive X-ray spectroscopy (STEM-EDX) elemental maps showing homogeneously alloyed $Pd_{13}Au_{87}$ NPs in $Pd_{13}Au_{87}/SiO_2$-RCT and $Pd_{13}Au_{87}/TiO_2$-RCT catalysts. White dashed circle is a guide to the eye. (d) TEM images of non-embedded $Pd_{13}Au_{87}/SiO_2$-attached and $Pd_{13}Au_{87}/TiO_2$-attached catalysts. NP size distributions of RCT and non-embedded catalysts are shown in the insets of (a) and (d), respectively, determined by measuring the diameters of 100 NPs per catalyst across multiple TEM images obtained in the same sitting.

Presence of Au/TiO_2 interfacial sites improves catalytic activity. RCT and non-embedded catalysts were evaluated for the liquid phase batch hydrogenation of benzaldehyde (BA) in isopropanol as our probe reaction, as guided by previous works from us and other researchers (28, 29, 38, 39). Our initial catalytic screening tests across the entire Pd_xAu_{100-x} NP composition range we prepared (x = 0, 4, 8, 10, 13, 100) indicated

that for both support chemistries, the $Pd_{13}Au_{87}$ NP composition exhibited the highest Pd mass-normalized activity (**Fig. S5a**), while the product distribution was unchanged across the entire bimetallic PdAu composition range (benzyl alcohol at >95% selectivity, toluene at <5% selectivity, with >95% total mass balance, **Fig. S5b–e**). Additionally, the activity and selectivity trends obtained in batch mode (**Fig. S5**) were reproducible in a fixed bed continuous flow mode too (**Fig. S6**). We separately comment that catalytic transfer hydrogenation from the isopropanol solvent to BA was absent in both SiO_2- and TiO_2-supported RCT catalysts as no BA conversion was detected when the reaction was performed in an inert Ar environment without H_2 gas (**Fig. S7**).

Most importantly, in the RCT catalysts after catalytic testing, we detected no physical changes to the macroscopic structure or NP size distribution (≈7 nm, **Fig. S8a**), and no migration or overgrowth of metal oxides onto segments of the NP surface exposed to reactants (**Fig. S8b**) that would otherwise restrict reactant accessibility. Together with the absence of metal leaching (**Table S1c**) and unchanged metal oxidation states (**Fig. S9**), our post-catalytic *ex situ* characterizations altogether confirm the high stability of the RCT catalysts, which we attribute to partial NP embedding in the support (28–30). The similar product selectivity and high RCT catalyst stability therefore allowed us to focus our analysis on the non-embedded and partially embedded RCT catalysts bearing the most active $Pd_{13}Au_{87}$ NPs to investigate the separate effects of support chemistry (SiO_2 *vs* TiO_2) or NP–support contact (non-embedded *vs* partially embedded RCT catalysts) on catalytic activity in batch mode in **Fig. 3a–b**. Note that catalytic results in **Fig. 3a–b** were obtained from three independent synthetic replicates of each catalyst for statistical analysis and to ensure that catalytic trends were reproducible.

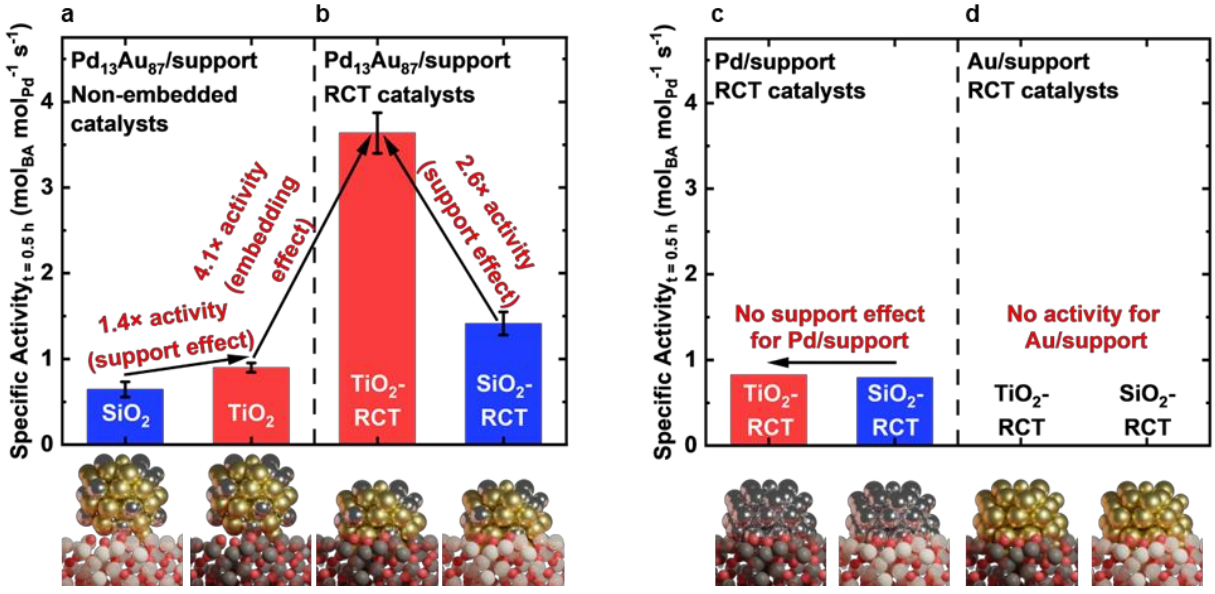

Fig. 3: Catalytic BA hydrogenation over non-embedded catalysts and partially embedded RCT catalysts. Bulk Pd mass-normalized specific activity in liquid phase BA batch hydrogenation over (a) non-embedded $Pd_{13}Au_{87}$/support-attached catalysts and (b)–(d) partially embedded RCT catalysts: (b) $Pd_{13}Au_{87}$/support-RCT, (c) Pd/support-RCT, and (d) Au/support-RCT (no activity detected). Specific activity data in (a)–(b) are presented as average ± standard deviation from three independent synthetic replicates of each catalyst. Statistical analysis of the support and embedding effects in (a)–(b) are provided in **Table S3**.

We first compared the non-embedded catalysts to determine the contribution of support chemistry on catalytic performance as quantified by the bulk Pd mass-normalized specific activity. $Pd_{13}Au_{87}/TiO_2$-attached was 1.4-fold more active than $Pd_{13}Au_{87}/SiO_2$-attached (**Fig. 3a**, *i.e.,* support effect) with statistical significance ($p = 0.01$, **Table S3**). As monometallic Au catalysts were inactive under similar reaction conditions (see **Fig. 3d**), we ascribed the non-zero reactivity of $Pd_{13}Au_{87}/SiO_2$-attached to the presence of surface Pd ensembles on the NP surface that activate H_2 and bind to BA, consistent with our earlier works (28–30). We point out that the 1.4-fold higher activity of $Pd_{13}Au_{87}/TiO_2$-attached, prepared in a similar manner as $Pd_{13}Au_{87}/SiO_2$-attached by depositing the same $Pd_{13}Au_{87}$ NPs but on a different support, suggests a non-innocent role of TiO_2 (*i.e.,* support effect), possibly due to additional BA binding at the NP–TiO_2 support interface, as described later in the next section.

Next, we compared the non-embedded (*i.e.,* NP-attached) and partially embedded RCT catalysts to study the effect(s) of NP embedding. $Pd_{13}Au_{87}/SiO_2$-attached (**Fig. 3a**) was half as active as $Pd_{13}Au_{87}/SiO_2$-RCT (**Fig. 3b**), likely due to unimpeded NP sintering and migration occurring in the NP-attached catalysts during catalytic testing (**Fig. S10**). Crucially, partial NP embedding in $Pd_{13}Au_{87}/TiO_2$-RCT enhanced the activity by a further 4.1-fold compared to $Pd_{13}Au_{87}/TiO_2$-attached (**Fig. 3a–b**, *i.e.,* embedding effect) with very high statistical significance ($p < 0.0001$, **Table S3**). This result was initially surprising to us as the RCT catalysts, in contrast to the non-embedded catalysts, exposed a much smaller fraction of its NP surface area to reactants (14). The activity enhancement from NP embedding into TiO_2 support (4.1-fold), together with a stronger support effect in the RCT catalysts (2.6-fold, **Fig. 3b**) compared to NP-attached catalysts (1.4-fold, **Fig. 3a**), imply the function of Au/TiO_2 interfacial sites for BA binding, whose contributions to catalytic activity was augmented by the increased NP–support interfacial perimeter. Our finding was substantiated by geometric calculations (**Note S1, Fig. S11**): from the NP-attached to partially embedded RCT catalysts, the NP–support interfacial perimeter increased 2.5-times, which necessarily leads to more Au/TiO_2 interfacial sites in the RCT catalysts as discussed and experimentally verified in the next section.

To ensure that the catalytic trends were not specific to the $Pd_{13}Au_{87}$ NP composition or due to the relatively poorer stability of the non-embedded catalysts, we tested SiO_2- and TiO_2-supported RCT catalysts with other NP compositions and ascertained that the support effect applied to all other bimetallic Pd_xAu_{100-x} NP compositions we prepared ($x = 4, 8, 10$;

Fig. S5a). Note that while we focus our discussion here on the most active $Pd_{13}Au_{87}$ NP composition, for the sake of completeness, the effect of NP composition on activity was studied as a side inquiry in **Note S2, Fig. S12–13**. Most crucially, the support effect was not present in the monometallic Pd or Au RCT catalysts (**Fig. 3c–d**). The similar activities (**Fig. 3c**) and chemical accessibilities (**Table S2**) of both Pd/SiO_2-RCT and Pd/TiO_2-RCT strongly indicate that *Au/TiO_2 interfacial sites, not Pd/TiO_2 interfacial sites and not TiO_2 surface sites alone, play the key role behind the enhanced activity of TiO_2-supported bimetallic catalysts as compared to SiO_2-supported catalysts.* Separately, the inactivity of both Au/SiO_2-RCT and Au/TiO_2-RCT in **Fig. 3d** imply that H_2 activation was sluggish over Au surfaces and Au/TiO_2 interfacial sites, in line with earlier reports (30, 40). In summary, our catalytic analyses establish that the activity enhancement derived from either changing the support from SiO_2 to TiO_2 (support effect) or from partial NP embedment of TiO_2-supported catalysts (embedding effect) are both intimately related to an increase in the number of Au/TiO_2 interfacial sites, whose role is discussed and validated below.

Benzaldehyde binds to Au/TiO_2 interfacial sites and Pd ensembles. To elucidate the underlying mechanism behind the support and embedding effects, we employed *in situ* surface-sensitive desorption analysis and theoretical calculations to investigate how BA binds to the Au/TiO_2 interface and other sites. BA temperature programmed desorption (TPD) was performed to identify the different BA binding sites and determine their relative binding strengths (41). Specifically, catalysts were cooled to 15 °C for BA adsorption and then heated to induce BA desorption, with each BA binding site exhibiting a distinct desorption temperature and combination of desorption product(s) related to its binding strength and geometry, respectively. We summarize the main results in **Fig. 4a–b**, with the full TPD data and analysis in **Fig. S14** and **Note S3**, respectively. BA was weakly adsorbed on SiO_2, as seen from the low temperature molecular desorption peaks (i) and (ii) in **Fig. 4a**. BA adsorption to Pd ensembles on the NP surface was assigned to a dissociative peak (iii) to benzene and CO, as this peak was exclusive to Pd-containing catalysts (top row of **Fig. 4a–b**) and that Pd is known to induce aldehyde decarbonylation (42–44). BA was adsorbed on TiO_2-supported catalysts in two different modes (**Fig. 4b**): a dissociative peak (iv) to toluene and a high temperature dissociative peak (v) to benzene and CO_2 corresponding to strong BA adsorption on TiO_2. We posit that toluene could have formed through BA carbonyl group decomposition at O vacancies in TiO_2, which created H adatoms to reduce adjacently adsorbed BA species, as alluded in a related work (45).

In the TPD data, we searched for peak shifts after NP incorporation to the support as an indication of NP–support interactions (46). Indeed, from TiO_2 to Au/TiO_2-RCT to $Pd_{13}Au_{87}/TiO_2$-RCT, the desorption temperature of peak (iv) decreased notably from 240 °C to 185 °C to 164 °C (**Fig. 4b**). This shift implies that the TiO_2 binding strength to BA was weakened by Au and Pd (albeit to a smaller extent). We also remark that in

$Pd_{13}Au_{87}/TiO_2$-RCT, peaks (iii) and (iv) overlap, signifying similar BA binding energies to Pd ensembles and Au/TiO_2 sites. This result agrees well with our theoretical calculations (**Fig. 4c, Fig. S15**) that depict comparable BA binding energies on Pd dimers in Au(111) (–1.1 eV, representing the most abundant Pd ensembles on $Pd_{13}Au_{87}$ NP surfaces based on **Fig. S12**) and at the Au/TiO_2 interface (–1.2 eV). Overall, surface-sensitive characterization and theoretical calculations identify moderate BA binding on Pd ensembles and Au/TiO_2 interfacial sites, and stronger BA binding on TiO_2 surfaces.

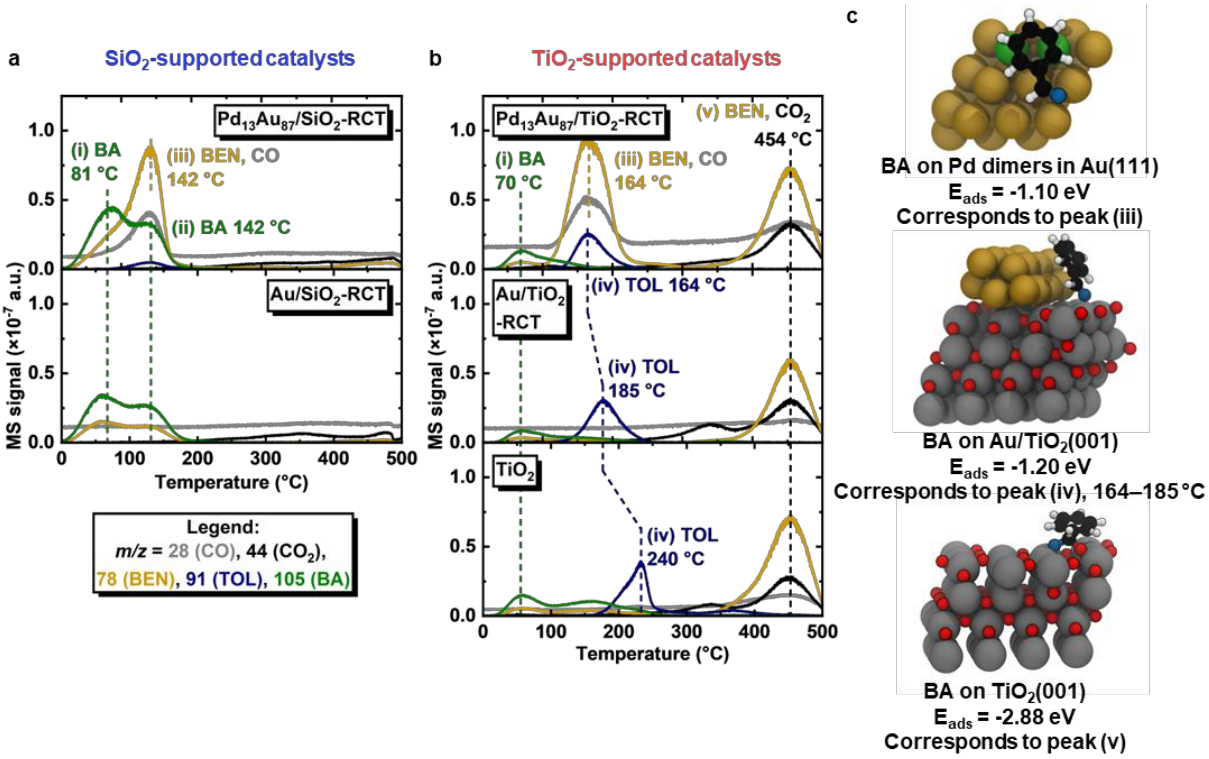

Fig. 4: Identification of BA binding sites on catalyst surfaces. BA TPD data for (a) SiO_2-supported RCT catalysts and (b) TiO_2-supported RCT catalysts. TPD signals were detected by on-line mass spectrometry using selected *m/z* channels for CO, CO_2, benzene (BEN), toluene (TOL), and BA. Full TPD results with data from additional *m/z* channels are shown in **Fig. S14** and discussed further in **Note S3**. Dashed lines indicate the major desorption peaks and are denoted as (i)–(v). (c) Optimized BA adsorption geometries and their calculated binding energies on various models from top to bottom: a pair of Pd dimers in Au(111), Au/TiO_2(001), and TiO_2(001). Additional structures and their calculated binding energies are shown in **Fig. S15**. Gold, green, grey, red, white spheres represent Au, Pd, Ti, O, H atoms respectively. The carbonyl O atom of BA was intentionally colored blue for differentiation from lattice O atoms of TiO_2. Note that the calculated –2.88 eV BA binding mode to TiO_2 in (c) involves the carbonyl C of BA binding to a lattice O in TiO_2, in agreement with the observed decarbonylation of BA to benzene and CO_2 as seen in peak (v) of (b).

As BA binds to both Pd ensemble sites and Au/TiO_2 interfacial sites, we quantified the ratio of these binding sites to estimate their relative contributions (*i.e.,* from the NP surface *vs* at the interface) to BA catalytic activity. Note that BA adsorbed on TiO_2 surfaces does not contribute appreciably to activity, evident from the similar activities of Pd/SiO_2-

RCT and Pd/TiO_2-RCT (**Fig. 3c**, with further discussions in **Note S4**). We used a temporal analysis of products (TAP) method predicated on the facile activation of O_2 on Pd ensembles (47, 48) and Au/TiO_2 interfacial sites (49, 50). Briefly, we pre-treated the catalysts with O_2, then introduced precise CO pulses to titrate off activated O adatoms at both sites as CO_2, whose quantity was proportional to the combined count of both sites (47, 48). Using TAP, $Pd_{13}Au_{87}$/TiO_2-RCT produced 5.2-times more CO_2 than $Pd_{13}Au_{87}$/SiO_2-RCT (**Fig. S16a–b, Table S4**). Assuming a comparable number of Pd ensemble sites in both catalysts, which should be valid given their similar chemical accessibility (**Table S2**), TAP revealed that in $Pd_{13}Au_{87}$/TiO_2-RCT, Au/TiO_2 interfacial sites were 4.2-times more abundant than Pd ensemble sites (**Fig. S16c**). TAP quantification also corroborates with CO chemisorption analyses that revealed a substantial 5.4-fold increase in the number of Au/TiO_2 interfacial sites from $Pd_{13}Au_{87}$/TiO_2-attached to $Pd_{13}Au_{87}$/TiO_2-RCT (**Fig. S17**). Therefore, we attribute the strong 4.1-fold embedding-induced activity enhancement (from $Pd_{13}Au_{87}$/TiO_2-attached to $Pd_{13}Au_{87}$/TiO_2-RCT), and the 2.6-fold support-induced activity enhancement (from $Pd_{13}Au_{87}$/SiO_2-RCT to $Pd_{13}Au_{87}$/TiO_2-RCT), as seen in **Fig. 3a–b**, primarily to the high abundance of Au/TiO_2 interfacial sites in the RCT catalysts, which facilitated additional BA binding and reaction at the NP–TiO_2 support interfacial perimeter.

Role of active sites in benzaldehyde hydrogenation. Considering all our findings, we propose the following roles of the different active sites for BA binding and H_2 activation—the two key elementary processes in catalytic BA hydrogenation (29, 39, 51)—to rationalize the observed catalytic trends. First, in $Pd_{13}Au_{87}$/SiO_2-attached, its non-zero activity stems from Pd ensembles on the NP surface performing both functions of BA binding and H_2 activation (**Fig. 5a**). Second, when the support was changed to TiO_2, a 1.4-fold higher activity was recorded for $Pd_{13}Au_{87}$/TiO_2-attached (*i.e,* support effect, **Fig. 3a**) due to additional BA binding on Au/TiO_2 interfacial sites, on top of BA binding to Pd ensembles (**Fig. 5b**). We remark that Au/TiO_2 interfacial sites activate H_2 poorly under our applied reaction conditions, as confirmed by the inactivity of Au/TiO_2-RCT (**Fig. 3d**) and in separate H_2–D_2 isotope exchange tests (**Fig. S18**) (31). Hence, we deduced that BA bound at the Au/TiO_2 interface was hydrogenated *via* H adatom spillover from adjacent Pd ensembles that activate H_2. This pathway is energetically favorable from theoretical calculations (**Fig. S19**): the calculated H adatom binding energy was much stronger at the Au/TiO_2 interface (–0.88 eV) than on a Au(111) surface (+0.14 eV). Third, partial NP entrenchment into the TiO_2 support enhanced catalytic activity by a further 4.1-fold (*i.e,* embedding effect, **Fig. 3b**) as the NP–support interfacial perimeter and by extension, the number of Au/TiO_2 interfacial sites, was increased by 5.4-times (**Fig. S17**), which augmented BA adsorption capacity and reaction at the interface (**Fig. 5c**). *Taken altogether, our results establish the importance of the Au/TiO_2 interface as an additional BA binding site principally responsible for the catalytic activity enhancements arising from both the*

support effects (from SiO_2 to TiO_2-supported bimetallic catalysts) or embedding effects (from the NP-attached to partially embedded TiO_2 bimetallic catalysts).

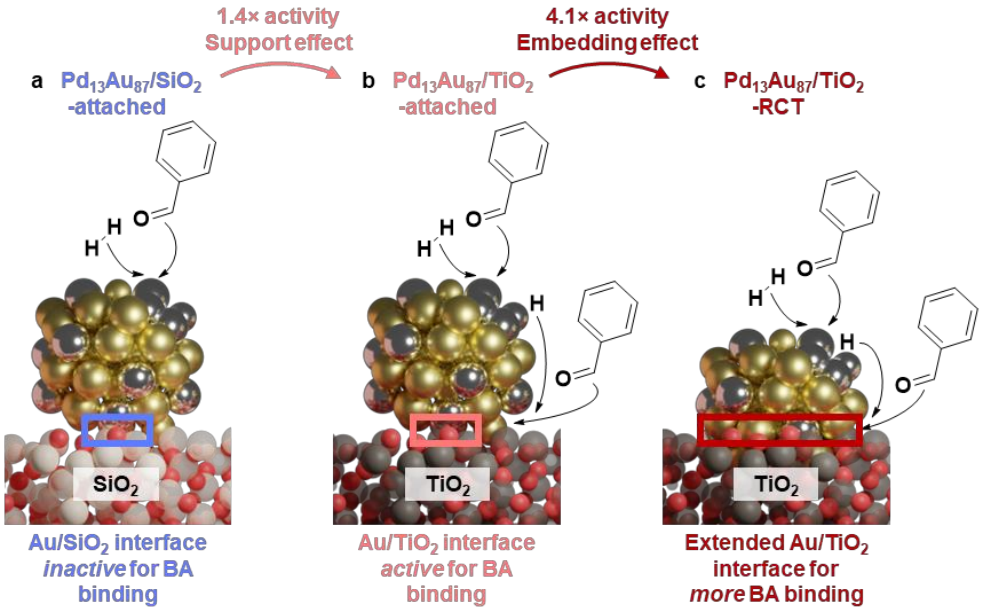

Fig. 5: Role of active sites in catalytic BA hydrogenation. Schematic describing BA binding and H_2 activation sites in (a) $Pd_{13}Au_{87}/SiO_2$-attached, (b) $Pd_{13}Au_{87}/TiO_2$-attached, and (c) $Pd_{13}Au_{87}/TiO_2$-RCT. Gold, silver, beige, grey, red spheres represent Au, Pd, Si, Ti, O atoms respectively. Boxes demarcate the NP–support interface. BA binding is facile on Pd ensembles and the Au/TiO_2 interface, but not on the Au/SiO_2 interface. H_2 activation is facile only on Pd ensembles. In (a), Pd ensembles on the NP surface perform both H_2 activation and BA binding to facilitate BA hydrogenation unassisted. In (b), BA not only binds to Pd ensembles, but also onto the Au/TiO_2 interface. Note that BA bound at the Au/TiO_2 interface undergoes hydrogenation assisted by H spillover from adjacent Pd ensembles on the NP surface that activate H_2, as H_2 activation was sluggish at the Au/TiO_2 interface under our applied reaction conditions. In (c), partial NP embedding increases the NP–support interfacial perimeter and accordingly, the number of Au/TiO_2 interfacial sites, to facilitate additional BA binding and further accelerate BA hydrogenation at the interface.

Conclusions

By adapting a modular RCT strategy, we decoupled the NP and support formation steps to partially embed pre-formed PdAu NPs of a fixed size in well-defined SiO_2 or TiO_2 supports (**Fig. 1a, 2a–c**), as verified by electron tomography in **Fig. S2** and in our earlier work (14). Unlike traditional impregnation, the RCT method enabled us to isolate and systematically investigate the roles of the NP–support interface without being confounded by concomitant changes to other potential catalytic descriptors (*e.g.,* NP size (9, 27, 28), proximity (29), or composition (30)). The RCT platform affords combinational flexibility to both the NP (26) and the metal oxide support chemistry (*e.g.,* alumina, ceria, zirconia) (25, 37, 52). Beyond a single support chemistry, mixed SiO_2–TiO_2 supports can be fabricated (53) to combine the mechanical stability of unreactive SiO_2 with the reactive

metal–TiO_2 interface. We further point out that the TiO_2 RCT support was formed using nanocrystals, which presents future opportunities to use shape-controlled nanocrystals to adjust the physicochemical properties of the support and modulate its interactions with catalytic NPs (35, 54). For instance, we envision that shape-controlled Cu_2O nanocrystals (55) can be attached to the templating colloids which are then co-assembled with colloidal ZnO nanocrystals to derive insights into the structural effects of Cu and refine industrial Cu/ZnO catalysts for catalytic CO_2 hydrogenation to methanol (56).

Crucially, the RCT method derives catalysts with partially embedded NPs (14), which increases the NP–support contact and accordingly, the number of interfacial sites, to amplify differences between catalysts with an active (Au/TiO_2) and inactive (Au/SiO_2) interface for reactant binding. In the RCT method, manipulating the wettability of the support precursor solution to the NPs and templating colloids can, in principle, enable control over NP embedding levels (14) and by extension, the NP–support interfacial perimeter. We also point out that in the RCT method, the NPs remain highly accessible to reactants (14). This feature contrasts with other inverted catalyst designs (21) whereby the overgrowth of metal oxides around NPs is contingent on the surface chemistry of both the NPs and support, which occasionally leads to excessive uncontrolled non-porous metal oxide overgrowth around NPs and their full encapsulation into the support (23, 57). The combination of high thermocatalytic stability, synthetic modularity, decoupled NP and support formation steps, and preserved reactant accessibility, strategically positions the RCT method as a model catalyst platform to elucidate unambiguous structure–property relationships that are otherwise challenging to investigate using traditional catalyst preparation methods (26).

We report a 1.4-fold activity enhancement in the non-embedded catalysts by changing the support from SiO_2 to TiO_2 (**Fig. 3a**, support effect), as the latter provided Au/TiO_2 interfacial sites to facilitate additional BA binding which we clarified using surface-sensitive desorption analyses and theoretical calculations (**Fig. 4b–c**). As Au/TiO_2 interfacial sites activate H_2 poorly, hydrogenation of BA bound at the Au/TiO_2 interface was assisted by H spillover from adjacent Pd ensembles on the NP surface that activate H_2 (**Fig. 5b**). Importantly, the activity of the $Pd_{13}Au_{87}/TiO_2$-attached catalyst was improved a further 4.1-fold by partial NP embedment (**Fig. 3a–b**, embedding effect), which created 5.4-times more Au/TiO_2 interfacial sites (**Fig. S17**) to increase BA adsorption capacity at the interface and accelerate BA hydrogenation (**Fig. 5c**). Our results demonstrate partial NP embedding as a synthetic strategy to accentuate catalytic contributions arising from metal–support interfaces (*i.e.,* interfacial catalysis), in addition to enhancing catalytic stability. While we illustrate this strategy on the Au/TiO_2 interface, which has broad catalytic relevance in selective hydrogenation, oxidation, and more (1–4), we anticipate that this concept can be readily extended to other crucial metal–support interfaces (*e.g.,*

Pt/CeO_2, Pd/In_2O_3, Rh/TiO_2, Cu/ZnO) to further enhance catalytic performance across a wide range of catalyst–reaction combinations (2, 24, 58). Finally, we also postulate that partial NP embedding can facilitate electron transport between NPs and active sites on conductive supports and their interfaces, which can be beneficially exploited to cooperatively enhance redox-mediated catalytic reactions on different active sites when conductive supports are involved (59).

Experimental

All materials and methods (catalyst synthesis, physical characterization, catalytic testing, and theoretical calculations) are described in detail in the Supporting Information. Briefly, to prepare the partially embedded Pd_xAu_{100-x}/SiO_2-RCT catalysts, NPs were first attached to amidine-functionalized polystyrene (PS) templating colloids to form NP-decorated raspberry colloids. The raspberry colloids were self-assembled to a colloidal crystal which was then infiltrated thrice with a pre-hydrolyzed SiO_2 sol-gel precursor, with a drying step (65 °C for 1 h) in between each infiltration. The infiltrated colloidal crystal was calcined in static air (500 °C for 2 h) to produce the Pd_xAu_{100-x}/SiO_2-RCT catalysts. To prepare the Pd_xAu_{100-x}/TiO_2-RCT catalysts, the same NP-decorated raspberry colloids were evenly mixed with a TiO_2 nanocrystal colloidal suspension and left undisturbed to co-assemble at 65 °C overnight in a convection oven. The co-assembled colloidal crystal was calcined in static air (500 °C for 2 h) to produce the Pd_xAu_{100-x}/TiO_2-RCT catalysts.

Acknowledgements

This work was supported by the U.S. Defense Threat Reduction Agency (DTRA) under award HDTRA12110016 (K.R.G.L., S.G., M.A., J.A.) and by the U.S. Department of Energy (DOE), Office of Science, Basic Energy Sciences under award DE-SC0012573 (S.K.K., J.A.). M.P.P. and J.E.S.v.d.H acknowledge the Starting PI Fund of the Electron Microscopy Center at Utrecht University. C.J.H. and M.M.M. are supported by U.S.–Israel Center for Fossil Fuels, administered by the Binational Industrial Research and Development (BIRD) foundation and the National Science Foundation (NSF) through grant CHE-2154952. K.R.G.L. acknowledges financial support from the Agency for Science, Technology and Research (A*STAR) Singapore National Science Scholarship (PhD). S.K.K. acknowledges the Swiss National Science Foundation (SNSF) for an Early Postdoc.Mobility fellowship (grant P2EZP2_199972). C.R. acknowledges funding *via* the Rowland Fellowship though the Rowland Institute at Harvard. Electron microscopy, CO chemisorption, infrared spectroscopy, and XPS analyses were performed at the Center for Nanoscale Systems (CNS), a member of the National Nanotechnology Coordinated Infrastructure Network (NNCI), which is supported by the NSF under NSF Electrical, Communications and Cyber Systems (ECCS) award 1541959. *In situ* DRIFTS and TPD analyses were conducted in the Reactor Engineering and Catalyst Testing (REACT)

Facility of the Northwestern University Center for Catalysis and Surface Science (CCSS), which is supported by the U.S. DOE under award DE-SC0001329. C.J.H. and M.M.M. acknowledge Tulane University with support in part from the high-performance computing (HPC) resources provided by Technology services at Tulane University as well as HPC resources provided by the Louisiana Optical Network Infrastructure (http://www.loni.org). K.R.G.L. and J.A. thank Prof. Cynthia Friend for the use of her laboratory facilities to conduct the catalytic hydrogenation reactions. K.R.G.L. and S.K.K. thank Prof. Robert Madix for initial discussions on this work. K.R.G.L. thanks Dr. Selim Alayoglu for assistance in setting up the TPD experiments.

References

1. R. T. K. Baker, S. J. Tauster, J. A. Dumesic, Eds., *Strong Metal-Support Interactions* (American Chemical Society, 1986).

2. T. W. van Deelen, C. Hernández Mejía, K. P. de Jong, Control of metal-support interactions in heterogeneous catalysts to enhance activity and selectivity. *Nat. Catal.* **2**, 955–970 (2019).

3. T. Ishida, T. Murayama, A. Taketoshi, M. Haruta, Importance of Size and Contact Structure of Gold Nanoparticles for the Genesis of Unique Catalytic Processes. *Chem. Rev.* **120**, 464–525 (2020).

4. D. Leybo, *et al.*, Metal–support interactions in metal oxide-supported atomic, cluster, and nanoparticle catalysis. *Chem. Soc. Rev.* **53**, 10450–10490 (2024).

5. M. Macino, *et al.*, Tuning of catalytic sites in Pt/TiO_2 catalysts for the chemoselective hydrogenation of 3-nitrostyrene. *Nat. Catal.* **2**, 873–881 (2019).

6. I. Ro, J. Resasco, P. Christopher, Approaches for Understanding and Controlling Interfacial Effects in Oxide-Supported Metal Catalysts. *ACS Catal.* **8**, 7368–7387 (2018).

7. A. Parastaev, *et al.*, Boosting CO_2 hydrogenation via size-dependent metal–support interactions in cobalt/ceria-based catalysts. *Nat. Catal.* **3**, 526–533 (2020).

8. M. Sankar, *et al.*, Role of the Support in Gold-Containing Nanoparticles as Heterogeneous Catalysts. *Chem. Rev.* **120**, 3890–3938 (2020).

9. N. E. Kolli, L. Delannoy, C. Louis, Bimetallic Au–Pd catalysts for selective hydrogenation of butadiene: Influence of the preparation method on catalytic properties. *J. Catal.* **297**, 79–92 (2013).

10. C. B. Paris, *et al.*, Impact of the Experimental Parameters on Catalytic Activity When Preparing Polymer Protected Bimetallic Nanoparticle Catalysts on Activated Carbon. *ACS Catal.* **12**, 4440–4454 (2022).

11. P. Munnik, P. E. de Jongh, K. P. de Jong, Recent Developments in the Synthesis of Supported Catalysts. *Chem. Rev.* **115**, 6687–6718 (2015).

12. E. D. Goodman, J. A. Schwalbe, M. Cargnello, Mechanistic Understanding and the Rational Design of Sinter-Resistant Heterogeneous Catalysts. *ACS Catal.* **7**, 7156–7173 (2017).

13. A. J. Martín, S. Mitchell, C. Mondelli, S. Jaydev, J. Pérez-Ramírez, Unifying views on catalyst deactivation. *Nat. Catal.* **5**, 854–866 (2022).

14. J. E. S. van der Hoeven, *et al.*, On the Origin of Sinter-Resistance and Catalyst Accessibility in Raspberry-Colloid-Templated Catalyst Design. *Adv. Funct. Mater.* **31**, 2106876 (2021).

15. J. Zhang, J. W. Medlin, Catalyst design using an inverse strategy: From mechanistic studies on inverted model catalysts to applications of oxide-coated metal nanoparticles. *Surf. Sci. Rep.* **73**, 117–152 (2018).

16. L. De Rogatis, *et al.*, Embedded Phases: A Way to Active and Stable Catalysts. *ChemSusChem* **3**, 24–42 (2010).

17. M. Bijl, *et al.*, Controlling nanoparticle placement in Au/TiO_2 inverse opal photocatalysts. *Nanoscale* **16**, 13867–13873 (2024).

18. J. Zhang, M.-R. Gao, J.-L. Luo, *In Situ* Exsolved Metal Nanoparticles: A Smart Approach for Optimization of Catalysts. *Chem. Mater.* **32**, 5424–5441 (2020).

19. D. Neagu, *et al.*, Nano-socketed nickel particles with enhanced coking resistance grown in situ by redox exsolution. *Nat. Commun.* **6**, 8120 (2015).

20. A. J. Carrillo, A. López-García, B. Delgado-Galicia, J. M. Serra, New trends in nanoparticle exsolution. *Chem. Commun.* **60**, 7987–8007 (2024).

21. S. Bhat, Y. J. Pagán-Torres, E. Nikolla, Strategies for Designing the Catalytic Environment Beyond the Active site of Heterogeneous Supported Metal Catalysts. *Top. Catal.* **66**, 1217–1243 (2023).

22. P. Wu, *et al.*, Harnessing strong metal–support interactions via a reverse route. *Nat. Commun.* **11**, 3042 (2020).

23. C. Gao, F. Lyu, Y. Yin, Encapsulated Metal Nanoparticles for Catalysis. *Chem. Rev.* **121**, 834–881 (2021).

24. M. Xu, *et al.*, Renaissance of Strong Metal–Support Interactions. *J. Am. Chem. Soc.* **146**, 2290–2307 (2024).

25. E. Shirman, *et al.*, Modular Design of Advanced Catalytic Materials Using Hybrid Organic-Inorganic Raspberry Particles. *Adv. Funct. Mater.* **28**, 1704559 (2018).

26. K. R. G. Lim, M. Aizenberg, J. Aizenberg, Colloidal Templating in Catalyst Design for Thermocatalysis. *J. Am. Chem. Soc.* **146**, 22103–22121 (2024).

27. L. A. Pretzer, *et al.*, Hydrodechlorination catalysis of Pd-on-Au nanoparticles varies with particle size. *J. Catal.* **298**, 206–217 (2013).

28. K. R. G. Lim, *et al.*, Deconvoluting the Individual Effects of Nanoparticle Proximity and Size in Thermocatalysis. *ACS Nano* **18**, 15958–15969 (2024).

29. K. R. G. Lim, *et al.*, Nanoparticle proximity controls selectivity in benzaldehyde hydrogenation. *Nat. Catal.* **7**, 172–184 (2024).

30. S. K. Kaiser, *et al.*, Identifying the Optimal Pd Ensemble Size in Dilute PdAu Alloy Nanomaterials for Benzaldehyde Hydrogenation. *ACS Catal.* **13**, 12092–12103 (2023).

31. J. E. S. van der Hoeven, *et al.*, Entropic Control of HD Exchange Rates over Dilute Pd-in-Au Alloy Nanoparticle Catalysts. *ACS Catal.* **11**, 6971–6981 (2021).

32. M. Luneau, *et al.*, Achieving High Selectivity for Alkyne Hydrogenation at High Conversions with Compositionally Optimized PdAu Nanoparticle Catalysts in Raspberry Colloid-Templated SiO_2. *ACS Catal.* **10**, 441–450 (2020).

33. A. Corma, P. Serna, Chemoselective Hydrogenation of Nitro Compounds with Supported Gold Catalysts. *Science* **313**, 332–334 (2006).

34. M. Boronat, *et al.*, A Molecular Mechanism for the Chemoselective Hydrogenation of Substituted Nitroaromatics with Nanoparticles of Gold on TiO_2 Catalysts: A Cooperative Effect between Gold and the Support. *J. Am. Chem. Soc.* **129**, 16230–16237 (2007).

35. J. H. Han, *et al.*, Highly Ordered Inverse Opal Structures Synthesized from Shape-Controlled Nanocrystal Building Blocks. *Angew. Chem. Int. Ed.* **61**, e202111048 (2022).

36. P. K. Routh, *et al.*, Restructuring dynamics of surface species in bimetallic nanoparticles probed by modulation excitation spectroscopy. *Nat. Commun.* **15**, 6736 (2024).

37. T. Shirman, *et al.*, Raspberry colloid-templated approach for the synthesis of palladium-based oxidation catalysts with enhanced hydrothermal stability and low-temperature activity. *Catal. Today* **360**, 241–251 (2021).

38. D. Procházková, P. Zámostný, M. Bejblová, L. Červený, J. Čejka, Hydrodeoxygenation of aldehydes catalyzed by supported palladium catalysts. *Appl. Catal. A: Gen.* **332**, 56–64 (2007).

39. Y. Song, *et al.*, Hydrogenation of benzaldehyde via electrocatalysis and thermal catalysis on carbon-supported metals. *J. Catal.* **359**, 68–75 (2018).

40. N. Dimitratos, *et al.*, Strategies to improve hydrogen activation on gold catalysts. *Nat. Rev. Chem.* **8**, 195–210 (2024).

41. J. P. H. Li, M. Stockenhuber, A temperature programmed desorption study of the interaction of ethyl cyanoacetate and benzaldehyde on metal oxide surfaces. *Catal. Today* **245**, 108–115 (2015).

42. J. L. Davis, M. A. Barteau, Polymerization and decarbonylation reactions of aldehydes on the Pd(111) surface. *J. Am. Chem. Soc.* **111**, 1782–1792 (1989).

43. R. Shekhar, M. A. Barteau, R. V. Plank, J. M. Vohs, Adsorption and Reaction of Aldehydes on Pd Surfaces. *J. Phys. Chem. B* **101**, 7939–7951 (1997).

44. R. M. Williams, J. W. Medlin, Benzyl Alcohol Oxidation on Pd(111): Aromatic Binding Effects on Alcohol Reactivity. *Langmuir* **30**, 4642–4653 (2014).

45. H. Idriss, K. S. Kim, M. A. Barteau, Surface-dependent pathways for formaldehyde oxidation and reduction on TiO_2(001). *Surf. Sci.* **262**, 113–127 (1992).

46. J. H. Kang, E. W. Shin, W. J. Kim, J. D. Park, S. H. Moon, Selective Hydrogenation of Acetylene on TiO_2-Added Pd Catalysts. *J. Catal.* **208**, 310–320 (2002).

47. M. Karatok, R. J. Madix, J. E. S. van der Hoeven, J. Aizenberg, C. Reece, Quantifying oxygen induced surface enrichment of a dilute PdAu alloy catalyst. *Catal. Sci. Technol.* **11**, 7530–7534 (2021).

48. T.-S. Kim, C. R. O'Connor, C. Reece, Interrogating site dependent kinetics over SiO_2-supported Pt nanoparticles. *Nat. Commun.* **15**, 2074 (2024).

49. M. Kotobuki, R. Leppelt, D. A. Hansgen, D. Widmann, R. J. Behm, Reactive oxygen on a Au/TiO_2 supported catalyst. *J. Catal.* **264**, 67–76 (2009).

50. I. X. Green, W. Tang, M. Neurock, J. T. Yates, Spectroscopic Observation of Dual Catalytic Sites During Oxidation of CO on a Au/TiO_2 Catalyst. *Science* **333**, 736–739 (2011).

51. G. Cheng, *et al.*, Critical role of solvent-modulated hydrogen-binding strength in the catalytic hydrogenation of benzaldehyde on palladium. *Nat. Catal.* **4**, 976–985 (2021).

52. J. E. S. Van Der Hoeven, A. V. Shneidman, N. J. Nicolas, J. Aizenberg, Evaporation-Induced Self-Assembly of Metal Oxide Inverse Opals: From Synthesis to Applications. *Acc. Chem. Res.* **55**, 1809–1820 (2022).

53. K. R. Phillips, *et al.*, Silica–titania hybrids for structurally robust inverse opals with controllable refractive index. *J. Mater. Chem. C* **8**, 109–116 (2020).

54. Y. Zhang, *et al.*, Structure Sensitivity of Au-TiO_2 Strong Metal–Support Interactions. *Angew. Chem. Int. Ed.* **60**, 12074–12081 (2021).

55. Z. Zhang, *et al.*, The active sites of Cu–ZnO catalysts for water gas shift and CO hydrogenation reactions. *Nat. Commun.* **12**, 4331 (2021).

56. S. Navarro-Jaén, *et al.*, Highlights and challenges in the selective reduction of carbon dioxide to methanol. *Nat. Rev. Chem.* **5**, 564–579 (2021).

57. W. Ke, X. Qin, Y. Vazquez, I. Lee, F. Zaera, Direct characterization of interface sites in Au/TiO_2 catalysts prepared using atomic layer deposition. *Chem Catal.* **4**, 100977 (2024).

58. T. Pu, W. Zhang, M. Zhu, Engineering Heterogeneous Catalysis with Strong Metal–Support Interactions: Characterization, Theory and Manipulation. *Angew. Chem. Int. Ed.* **62**, e202212278 (2023).

59. X. Huang, *et al.*, Au–Pd separation enhances bimetallic catalysis of alcohol oxidation. *Nature* **603**, 271–275 (2022).